


Valorisation of sugar cane bagasse using hydrothermal carbonisation in the preparation of magnetic carbon nanocomposite in a single-step synthesis applied to chromium adsorption

Márcio J Laranja,^a Francisco HS Júnior,^{b,c} Gabriela A Nogueira,^a Lais HS Vieira,^b Naiara C Oliveira,^b João M Soares,^d Carlos HN Cordeiro,^d Larissa Otubo,^e Altair B Moreira,^a Odair P Ferreira^{b,f*}  and Márcia C Bisinoti^a



Abstract

BACKGROUND: Sugar cane bagasse (SB) is a by-product of the sugar cane industry, and is obtained on a large scale. In this paper, SB was used as a source of carbon for preparing a magnetic carbon nanocomposite (MCN-SB) through one-step hydrothermal carbonisation (HTC), in the presence of iron (III) nitrate. By way of comparison, SB was replaced by glucose in HTC (MCN-GLU), and a thermal treatment of this material was then performed under an N₂ atmosphere (MCN-GLU-HT). The physical and chemical properties of the nanocomposites were assessed, and the magnetic samples were applied as adsorbents.

RESULTS: MCN-SB and MCN-GLU are composed of iron oxide nanoparticles embedded in carbonaceous matrix which also contain oxygenated groups. The MCN-SB sample was already magnetic after HTC, showing a magnetization saturation (M_s) of 5.0 emu g⁻¹, due to the presence of magnetite, whereas MCN-GLU consisted of hematite and required additional thermal treatment (HT) to acquire magnetic properties, with MCN-GLU-HT showing an M_s of 30.5 emu g⁻¹. In turn, the mesoporous structure and higher specific surface area (SSA) of MCN-GLU-HT (SSA 90 m² g⁻¹) than MCN-SB (SSA 53 m² g⁻¹) was a causative factor for its higher capacity of hexavalent chromium [Cr (VI)] removal (939 µg g⁻¹), when compared to MCN-SB (768 µg g⁻¹), which has a nonporous structure.

CONCLUSION: The results suggest that SB can be reused, by means of HTC, for the preparation of a magnetically recoverable adsorbent, showing good adsorption properties.

© 2022 Society of Chemical Industry (SCI).

Supporting information may be found in the online version of this article.

Keywords: biomass; transformation; environmental chemistry; characterisation

INTRODUCTION

In Brazil, from the 1970s onwards, the federal government had a national programme (Proálcool) aimed at gradually replacing oil (a nonrenewable fossil fuel) with ethanol obtained from

renewable sources such as sugar cane, motivated mainly by the oil crisis. Since then, the sugar cane industry has developed robustly, making Brazil the second largest ethanol producer in the world.¹ In this process, sugar cane bagasse (SB) is the main

* Correspondence to: OP Ferreira, Laboratório de Materiais Funcionais Avançados (LaMFA), Departamento de Física, Universidade Federal do Ceará (UFC), Campus do Pici, mailbox 3151, 60355-636 Fortaleza, Ceará State, Brazil. E-mail: opferreira@fisica.ufc.br

a Laboratório de Estudos em Ciências Ambientais (LECA), Departamento de Química e Ciências Ambientais, Universidade Estadual Paulista (Unesp), Instituto de Biociências, Letras e Ciências Exatas, São José do Rio Preto, Brazil

b Laboratório de Materiais Funcionais Avançados (LaMFA), Departamento de Física, Universidade Federal do Ceará, Fortaleza, Brazil

c Departamento de Ensino, Instituto Federal do Ceará, Limoeiro do Norte, Brazil

d Centro de Síntese e Análise de Materiais Avançados (CSAMA), Departamento de Física, Universidade do Estado do Rio Grande do Norte, Mossoró, Brazil

e Instituto de Pesquisas Energéticas e Nucleares, IPEN/CNEN-SP, Cidade Universitária, São Paulo, Brazil

f Departamento de Química, Universidade Estadual de Londrina (UEL), Londrina, Brazil

solid by-product, obtained after grinding the fibre to extract the juice. Large quantities are obtained annually in each harvest, and require proper disposal and treatment, to avoid causing environmental pollution. Some attempts at reuse have been made, such as the production of energy by burning in boilers, cellulosic ethanol, bioplastics and as animal feed for confined cattle.^{2,3} Even so, there is still some excess that is not used, which underlies the need for work to add value to this material.

Magnetic carbon nanocomposites (MCN) are nanomaterials that have attracted researchers' interest owing to their unique and adjustable properties, which make them suitable for application in many areas such as energy, catalysis, medical sciences and adsorption.⁴⁻⁷ Different magnetic sources, such as iron-, nickel- and cobalt-based compounds have been used in MCN synthesis,⁸ whereas a wide variety of carbon (C) sources have been studied, such as glucose, cellulose and melamine.⁹⁻¹¹ Recently, several works have shown the feasibility of using agroindustrial wastes (peanut hulls, sesame oil cake, sugar cane bagasse) as alternatives, because these materials have low cost and large availability, and moreover, to allow the resource recovery from waste, along with reducing the environmental impact of agroindustrial activities.¹²⁻¹⁴

In order to produce MCNs, many processing methods have been used, and here we highlight pre-coating/postcoating pyrolysis, chemical co-precipitation, microwave heating, ultrasonication and hydrothermal carbonisation (HTC).^{12,15-18} A two-step method was employed for converting termite faeces and ferric chloride into a magnetic C, by an sulfuric acid (H_2SO_4) treatment followed by pre-coating pyrolysis, which was applied for hexavalent chromium [Cr (VI)] removal.¹⁹ Recently, hydrothermal carbonisation, a low-temperature thermochemical method of biomass conversion, which takes place in aqueous media, has gained prominence in the synthesis of C-rich materials using agricultural residues as raw precursors, owing to the possibility of using water as a reagent and solvent in the process, also enabling the use of acids, salts and bases to modify the material's characteristics.²⁰

In the same way, HTC also has been used as a synthesis method for obtaining C-based magnetic adsorbents, owing to the multifunctional aspect of its structure, which is the result of porosity and the presence of functional groups on its carbonaceous surface, thereby providing adsorption sites, combined with the magnetic properties of the iron oxide nanoparticles (γ - Fe_2O_3 – maghaemite or Fe_3O_4 – magnetite) incorporated into the material,^{9,21,22} thereby helping the easy recovery of adsorbent from the solution. In addition, the presence of a carbonaceous layer covering the magnetic phase gives protection from oxidation in acidic media,²³ expanding its range of applications as an adsorbent.

In general, centrifugation and filtration methods are used to separate the adsorbent material (solid phase) from aqueous solution. These applications are time-consuming and costly. Compared with these traditional methods, the magnetic separation method is an efficient, fast and economic method for the separation of magnetic adsorbents from the solutions after the adsorption treatment of pollutant is completed. The separation of nonmagnetic adsorbents from sample solution after adsorption is very difficult and also time-consuming. This problem can be solved by the incorporation of magnetic nanoparticles on the surfaces of nanocomposite adsorbents and then by using a magnet. In addition, Fe_3O_4 nanoparticles are the most widely used materials in the preparation of magnetic nanocomposite adsorbents

owing to their unique properties such as chemical stability, uniform particle size and biocompatibility.

Most works can get magnetic C through HTC only with procedures involving two or more steps. For instance, a magnetic C composite was obtained by the thermal treatment of hydrochar from *Salix psammophila* which had been treated with a mixture of iron (III) chloride ($FeCl_3$) and zinc chloride ($ZnCl_2$) and applied as adsorbent of triclosan.²⁴ In the specialised literature, there are few papers reporting MCN preparation using a one-step HTC method,¹⁶ and whatismore these cases involve the use of additives along with iron salt and biomass. One of these works produced an amino-functionalised magnetic C-based adsorbent through a mild one-step hydrothermal method using peanut hull waste, in the presence of $FeCl_3$ and hexamethylenediamine, for removal of Cr (VI). As far as we know, the preparation of MCN using only SB and iron salts, without any additive, has never been reported by HTC.

This study aims to develop a simpler and eco-friendly process for MCN preparation. We are proposing to use SB as C source in the HTC process along with iron (III) nitrate. The compositional, morphological, textural and magnetic properties of the nanocomposite obtained from SB were investigated and compared with the properties of the nanocomposite obtained from HTC of glucose in the presence of iron (III) nitrate followed by thermal treatment at 500 °C in a flow of N_2 . Likewise, as a way of complementing the characterization of the magnetic nanocomposites, batch adsorption studies were performed using Cr (VI).

MATERIALS AND METHODS

Chemicals and materials

For production of MCN, two different sources of C were used as raw materials: glucose, a monosaccharide, and SB, a lignocellulosic biomass. Anhydrous glucose ($C_6H_{12}O_6$, 99.98%) was purchased from Vetec (Brazil), whereas SB was supplied by a sugar cane industry in São Paulo state. The collected sample was registered on the National System for the Management of Genetic Heritage and Associated Traditional Knowledge (SisGen), under no. A0018C2. The SB was washed with water, dried at 100 °C for 12 h, ground in a knife mill (Marconi, MA 340), sifted (<0.5 mm; Granutest) and then stored at room temperature. $[Fe(NO_3)_3] \cdot 9H_2O$ (98.0%; Synth, Brazil) was employed as iron source in the step of MCN synthesis. 1,5-diphenylcarbazide (98.0%; Vetec), phthalic anhydride (99.0%, Vetec), H_2SO_4 (96.0%; Synth), $K_2Cr_2O_7$ (1000 mg L^{-1} ; Specsol®, Brazil) and anhydrous C_2H_5OH (98.0%; Sigma-Aldrich, USA) were employed in the Cr (VI) determination. HCl (37.0%; Synth) and NaOH (98.0%; Synth) were used for pH adjustment in batch adsorption experiments. All experiments were carried out using ultrapure milli-Q® water (18.2 M Ω cm^{-1}).

Production of MCNs

Preparation of MCN from glucose

The preparation of MCN from glucose followed a two-step process: (i) HTC followed by (ii) thermal treatment in a tubular furnace, where all procedures were performed as indicated previously.²⁵ To start with, in order to produce a nanocomposite with a nominal Fe/C ratio (w/w) of 23%, glucose (0.90 g) and $[Fe(NO_3)_3] \cdot 9H_2O$ (0.60 g) were added to 40 mL ultrapure water. The solution was ultrasonicated for 15 min (model EW 08895-49; Cole-Parmer®) and then the pH was measured at ≈ 2.0 . Then, the solution was transferred to a Teflon®-lined stainless-steel autoclave (60-mL capacity), and heated up to 190 ± 10 °C in a muffle

furnace (model 7000; EDG Equipment) for 9 h. At the end of the process, the reactor was naturally cooled down to room temperature, and the solid–liquid separation then was carried out through centrifugation (Excelsa II, model 206 BL; Fanem®) at 3200 rpm during 10 min. The solid product was washed with ultrapure water until the pH of the supernatant was ≈ 5 , and then oven-dried (70 ± 10 °C) for 24 h. The brown powder (MCN-GLU) obtained was not magnetic. Next, the nonmagnetic nanocomposite was subjected to thermal treatment using a tubular furnace (model FTHI/20; EDG Equipment), under moderate N₂ flow at 500 °C with heating rate of 10 °C min⁻¹ and residence time of 2 h. After cooling under a N₂ environment, the sample was stored and given the name of MCN-GLU-HT. The black powder obtained was magnetic.

Preparation of MCN from SB

Unlike the procedure described above for glucose, the preparation of MCN from SB was made in one step, by simultaneous carbonisation and magnetic phase formation. Dried bagasse was weighed in a beaker (3.00 g) and then mixed with [Fe(NO₃)₃]·9H₂O (1.80 g) and 60 mL ultrapure water. The suspension was magnetically stirred (model 752; Fisatom®) for 20 min and the pH was measured at ≈ 2.0 . This suspension then was transferred into a 100-mL reactor (series 4598; Parr, Moline, IL, USA). The HTC was conducted at 250 °C with a residence time of 6 h. The reaction medium was stirred continuously at 160 rpm. At the end of the process, the reactor was cooled down naturally and the solid product was separated by filtration under reduced pressure. The product was washed with ultrapure water until the pH of supernatant reached ≈ 7 and then was oven-dried (model N1040; Tecnik) at 70 ± 10 °C for 24 h, resulting in a magnetic brown powder which was denoted (MCN-SB). The dried solid product was macerated, sifted and stored. For the purpose of comparison, a material was produced by HTC, from SB, in the absence of iron (III) nitrate, under the same conditions described above, here referred to as HC-SB.

Physicochemical characterisation of MCN

The composition of MCN was evaluated by thermogravimetric analysis (TGA), carried out in STA equipment (449 F3; Netzsch) from 30 to 800 °C, under an air flow of 50 mL min⁻¹ and with a heating rate of 10 °C min⁻¹. The mass of the sample used was ≈ 10 mg.

A structural analysis of inorganic phases was carried out by powder X-Ray diffraction (XRD) analysis (model D8 Advanced; Bruker), using Cu-K- α radiation ($\lambda = 0.154$ nm), generated at 40 mA and 40 kV over an angular range of 5°–85° (2θ) using steps of 0.02° s⁻¹. The phase was identified with the use of the X'Pert Highscore Plus software (Rigaku). For specifying iron-oxide structures, Rietveld refinement was applied to these XRD data, using MAUD (Material Analysis Using Diffraction) open-source software.

Magnetic measurements were made using a homemade vibrating sample magnetometer (VSM) at room temperature in an applied magnetic field of ± 12 KOe (kiloersted). The electron paramagnetic resonance spectrum (EPR) was measured at room temperature using a Bruker EMXmicro apparatus. The instrument was operated under the following conditions: microwave frequency 9.695 and 9.715 GHz; power 152.7 and 187.2 mW; phase modulation 0° and 210°; conversion time 61 and 119 ms; number of scans 1 and 2.

Attenuated total reflection Fourier transform infrared spectroscopy (ATR-FTIR) was carried out to identify the functional groups on the carbonaceous material, with the spectra being recorded

on spectrometers (model Vertex 70 V; Bruker) equipped with a Platinum ATR accessory and (Spectrum Two UATR; Perkin Elmer) equipped with diamond ATR module. Around 5–10 mg of dry sample was placed in the ATR accessory. The spectra were obtained in the mid-infrared region (400–4000 cm⁻¹) with resolution of 4 cm⁻¹ and 128 scans.

Nitrogen adsorption–desorption analyses were carried out with a sorptometer (Belsorp mini II; BEL Japan, Inc.). The samples were outgassed at 105 °C for 14 h under a flow of N₂. The specific surface area (S_{BET}) was calculated using the Brunauer–Emmett–Teller (BET) method. The total pore volume was calculated by the Barrett–Joyner–Halenda (BJH) method.

The morphology of the samples was observed using scanning electron microscopy (SEM) and transmission electron microscopy (TEM). The SEM images were obtained using Quanta 450 FEG and Inspec S50 microscopes, (FEI; Thermo Fisher Scientific). For this, crushed and sifted samples were pulverised on C tape attached to aluminium sample holders and coated with thin gold film, by sputtering (ES QT150; Quorum Technologies, Lewes, UK). For the TEM images, the sample powders were suspended in isopropanol and dripped on a collodium-coated copper grid. For elemental mapping, energy dispersive X-ray spectroscopy (EDS) was recorded using an X-ray detector (model 150; Oxford Instruments, Abingdon, UK) coupled to Quanta 450 FEG microscope.

Batch adsorption studies

The batch adsorption studies were performed using an adsorbent dosage of 0.5 g L⁻¹. For kinetic experiments, the Cr (VI) solutions (1.0 mg L⁻¹) were constantly shaken at 100 rpm for different time intervals (0, 60, 120, 240, 420, 600 and 1440 min) using an orbital shaker. Adsorption isotherms were obtained in the Cr (VI) concentration range from 0.3 to 1.1 mg L⁻¹ for 10 h. The pH of the suspension was previously adjusted to 5.0 using HCl or NaOH solution (0.1 mol L⁻¹). The amount of Cr (VI) removed by MCN samples ($\mu\text{g g}^{-1}$) was calculated based on Eqns (1) and (2):

$$Q_e = \frac{(C_0 - C_e) * V}{m} \quad (1)$$

$$R (\%) = \frac{(C_0 - C_e) * 100}{C_0} \quad (2)$$

where Q_e is the adsorption capacity of MCN; C_0 and C_e are the initial and equilibrium concentration of Cr (VI) (mg L⁻¹), respectively; V is the solution volume (mL); m is the adsorbent mass used; and $R (\%)$ is the removal efficiency.

In order to verify the effect of contact time in the chromium adsorption on the magnetic nanocomposites, the data were fitted with nonlinear kinetic models: pseudo-first-order (PFO), pseudo-second-order (PSO) and Elovich. In the same way, for evaluate the effect of chromium concentration, the data were fitted to the nonlinear models of Langmuir and Freundlich.

Determination of Cr (VI)

The standard (10.0 mg L⁻¹) and work (0.1–1.1 mg L⁻¹) solutions were obtained by dilution of Cr (VI) stock solution (1000.0 mg L⁻¹; Specscol®) using ultrapure water. The content of Cr (VI) was established by using the colorimetric method (3500-Cr.B),²⁶ using 1,5-diphenylcarbazide 0.50% w/v in anhydrous ethanol and H₂SO₄ (1.20 mol L⁻¹). The measurements were

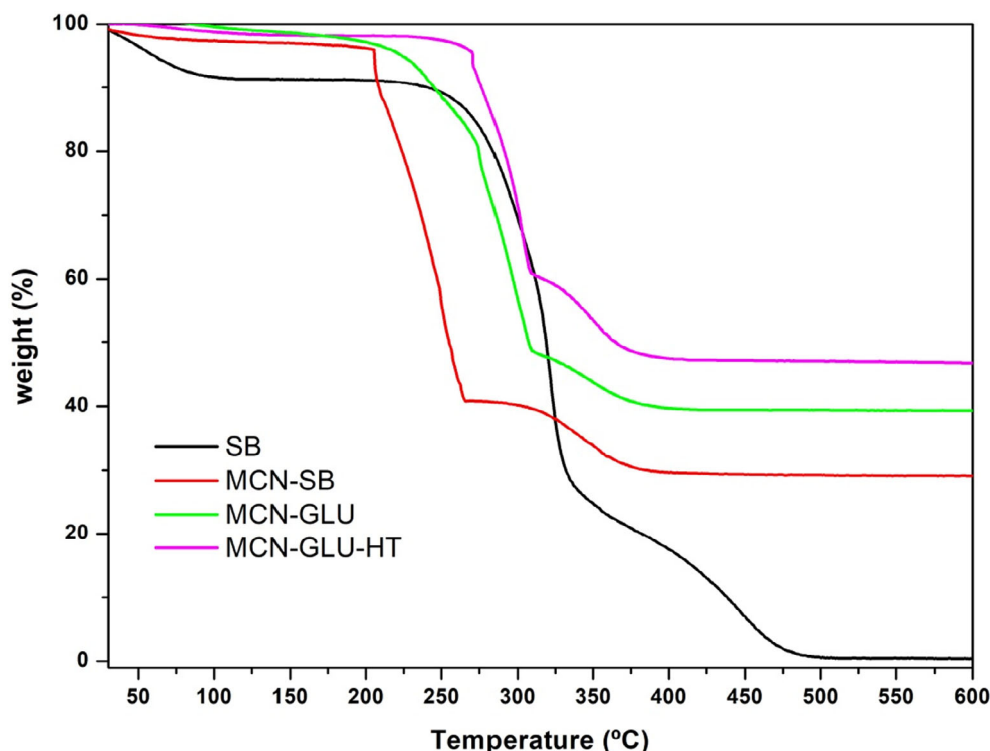


Figure 1. TGA curves of SB, nonmagnetic nanocomposite prepared from glucose (MCN-GLU), and magnetic nanocomposites prepared from SB (MCN-SB) and glucose (MCN-GLU-HT). Source File: ORIGIN PRO 8.5.

carried out using a UV-visible spectrophotometer (UV-2600; Shimadzu®, Kyoto, Japan) at $\lambda = 540$ nm.

RESULTS AND DISCUSSION

Characterisation of the MCNs

Compositional investigation

The TGA analyses (Fig. 1) were carried out in air, aiming to study the thermal decomposition of the carbonaceous matrix and to quantify the inorganic contents. It can be seen that TGA curves contain two distinct weight-loss steps: (i) removal of adsorbed water (30–150 °C) and (ii) combustion of carbonaceous matrix (200–400 °C), with only the inorganic fraction at >500 °C remaining. An exception was observed in the case of SB, in which the second step finished only at 500 °C.

In the first step, the SB lost $\approx 8.7\%$ of its mass until 150 °C (Table 1; Fig. 1). This thermal event could be attributed to the elimination of adsorbed water on the lignocellulosic fibre. After HTC, the water content in the materials decreased. For MCN-SB, we clearly observed a weight loss of 2.9%, whereas for nonmagnetic nanocomposite MCN-GLU the weight loss observed was 1.7%. In the HTC process, a series of reactions occurs to convert the biomass and monosaccharides into a C-rich solid,²⁷ involving the elimination of water (dehydration and condensation). MCN-GLU-HT has shown the lowest water content (1.4%), probably due to the more hydrophobic character of this sample, having been heat-treated at 500 °C, thereby eliminating functional groups in the C matrix (see FTIR spectrum in Fig. 3).

As the temperature increased (from 150 up to 400 °C), degradation of the more volatile organic fraction began. The TGA profile of SB clearly showed its predominant organic composition, with

Table 1. Moisture, carbonaceous content, residue and calculated iron content of iron oxide carbonaceous nanocomposites (MCN-SB, MCN-GLU and MCN-GLU-HT) as obtained from TGA analysis

Samples	Moisture content ^a (%)	Carbonaceous content ^b (%)	TGA residue ^c (%)	Iron content ^d (%)
SB	8.7	90.6	0.4 ^e	0.0
MCN-SB	2.9	67.3	29.0	20.0
MCN-GLU	1.7	58.4	39.4	27.6
MCN-GLU-HT	1.4	51.2	48.0	34.0

^a measured as percentage of weight loss <150 °C;

^b percentage of weight loss between 150 and 400 °C;

^c obtained at 600 °C as Fe₂O₃ content for iron-oxide nanocomposites;

^d Obtained from %Fe = %Fe₂O₃/1.43;

^e SiO₂.

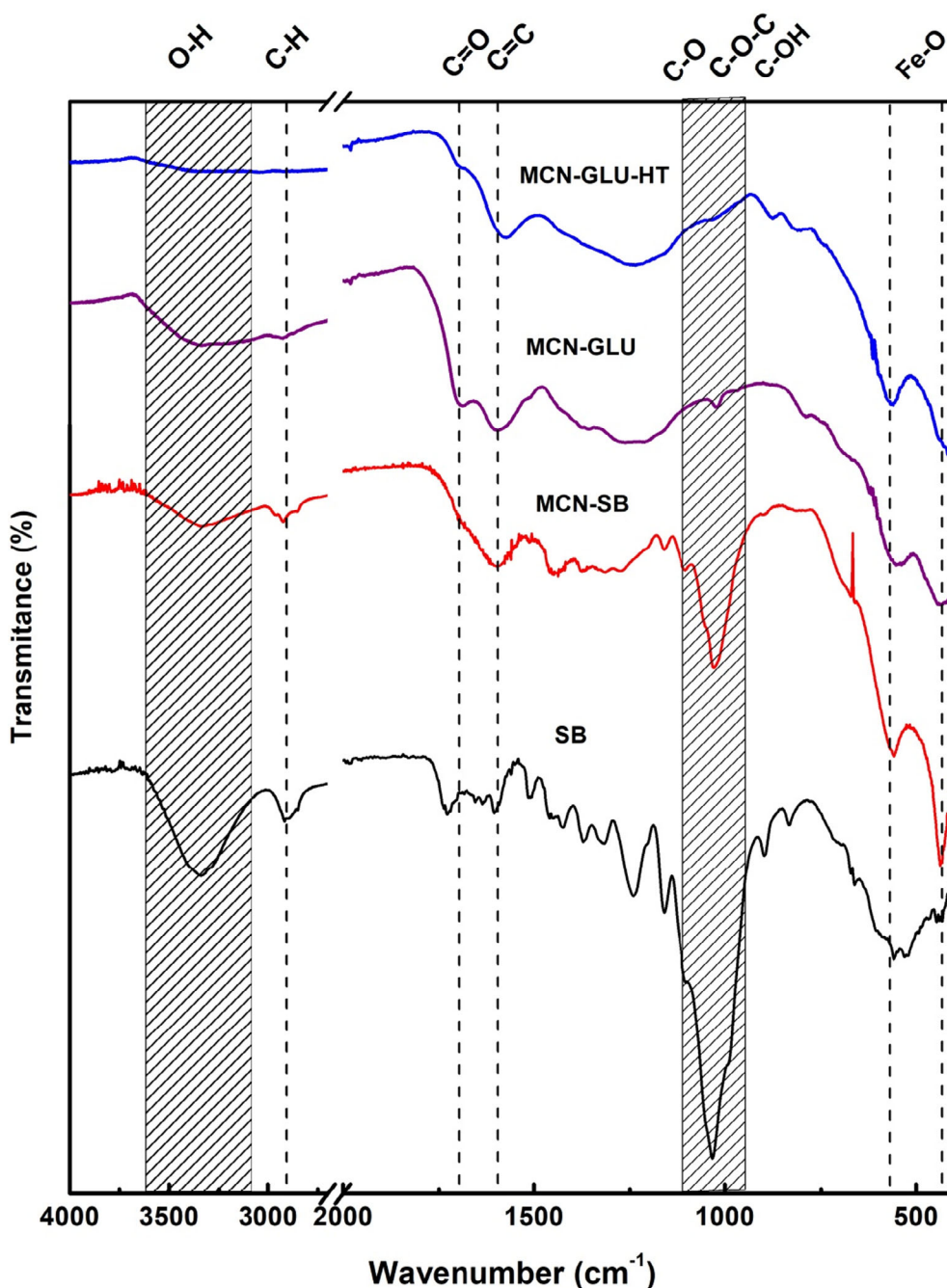


Figure 3. FTIR spectra of MCN-GLU-HT, MCN-GLU, MCN-SB and raw SB. Source File: ORIGIN PRO 8.5.

90.6% of organic content based on a lignocellulosic structure. The main components of the lignocellulosic structure were thermally degraded at different temperatures, with hemicellulose starting at >200 °C, cellulose at >240 °C and lignin at >280 °C²⁸ (see Table 1).

Looking at the nanocomposites, MCN-SB showed a sharp weight loss (68.1%), starting at 205 °C, which suggests that the carbonaceous matrix started to degrade at this temperature. However, MCN-GLU and MCN-GLU-HT showed lower thermal degradation (58.9% and 50.6%) in the range between 150 and 400 °C, which also started at higher temperatures (231 and 270 °C) than MCN-SB. The thermal stability of a material is related to the temperature at which its thermal decomposition begins.

The heat treatment of MCN-GLU at 500 °C probably allowed the creation of the first most graphitised domains, leading to an increase in the temperature of decomposition of the carbonaceous fraction of this sample. However, analysing the TGA profile of MCN-GLU, we can see that the degradation temperature of the glucose composite (MCN-GLU) was far higher than that of the composite from a lignocellulosic biomass (MCN-SB), even that hydrothermally treated at 250 °C. From these results, one can conclude that there was a difference in thermal stability of the different carbonaceous matrices, with $\text{MCN-SB} < \text{MCN-GLU} < \text{MCN-GLU-HT}$. The mass stability after 400 °C suggests that the carbonaceous matrix was completely decomposed by oxidation in air and the solid residual ashes were related to inorganic compounds (see

Table 1), also suggesting that iron oxides remained encapsulated in as prepared nanocomposites.¹³

From TGA curves (Fig. 1), one can observe that MCN-GLU-HT had a higher residue content (48.0%) than MCN-SB (29.0%) and MCN-GLU (39.4%). In the case of MCN-GLU and MCN-GLU-HT, these values could be assigned entirely for iron oxide phases, especially α - Fe_2O_3 , as only the hematite phase is stable at 600 °C²⁹ and also because of the intense red colour observed in the residue, which is characteristic of hematite. For SB, the ash content was more related to silicon oxide in biomass ($\approx 0.4\%$); as a consequence of its low value, this will not be taken into account for the calculation of the iron content in the nanocomposite prepared using this biomass.

Iron content was calculated according to TGA residue values (Table 1), whereas MCN-GLU-HT stood out with a higher Fe content (34.0%), whilst MCN-GLU (27.6%) and MCN-SB (20.0%) showed lower values. Thus, it was verified that the actual iron contents of MCN-SB and MCN-GLU were close to the nominal value of the Fe:C mass ratio predicted in the experimental scheme. Furthermore, the higher TGA residue obtained for MCN-GLU-HT suggests that part of the carbonaceous matrix was being degraded during thermal treatment at 500 °C, which helped to reduce the organic fraction and indirectly increase the Fe:C mass ratio in the nanocomposite, as other works have also reported.¹⁰

The HC-SB, MCN-SB, MCN-GLU and MCN-GLU-HT samples were also characterised by XRD as shown in Fig. 2. The XRD patterns of HC-SB and MCN-SB show two broad peaks with low intensity centred at 15.4 and 22.2° (2θ) superimposed onto an amorphous halo in the range of 10–30°. The two first peaks could be

attributed to cellulose present in the bagasse that was not completely degraded.³⁰ The amorphous halo is typical of structurally poorly ordered carbonaceous material, compatible with the presence of hydrothermal C.³¹ Additionally, in the XRD pattern for HC-SB it was possible to observe some additional peaks at 26.5 and 49.9° (2θ), which could be indexed to the crystalline phases of SiO_2 (ICSD no. 034925). This phase would have its origin in the used raw materials.³²

The XRD for the composites revealed some narrow and more intense peaks, which are related to the inorganic phases. The XRD pattern of MCN-GLU revealed diffraction peaks at 35.4°, 40.3°, 53.0°, 61.0° and 63.0° (2θ), as well as peaks at 18.2°, 45.7° and 47.0° (2θ), characteristic of hematite (α - Fe_2O_3 , ICSD no. 024791) and goethite (α - FeOOH , ICSD no. 28247) phases, respectively.³³ However, in the XRD pattern of MCN-GLU-HT it was possible to observe peaks attributed to the magnetite phase (Fe_3O_4 , ICSD no. 020596), which was probably related to heat treatment at 500 °C under the inert atmosphere, thus creating more favorable conditions for the reduction from Fe^{3+} to Fe^{2+} took place. One surprising result was observed in the XRD pattern for MCN-SB sample showing peaks that could be attributed to Fe_3O_4 and/or γ - Fe_2O_3 (ICSD no. 87119) phases, justifying its magnetic response in front of a magnet. It is well worth mentioning that the diffraction pattern of the magnetite and maghemite phases are very similar. However, the absence of some peaks at low angles suggests the absence of the maghemite phase.³⁴ We will return to this discussion in the section on EPR Spectroscopy.

The Rietveld refinements of the XRD patterns showed that both MCN-GLU-HT and MCN-SB have iron oxide nanoparticles with

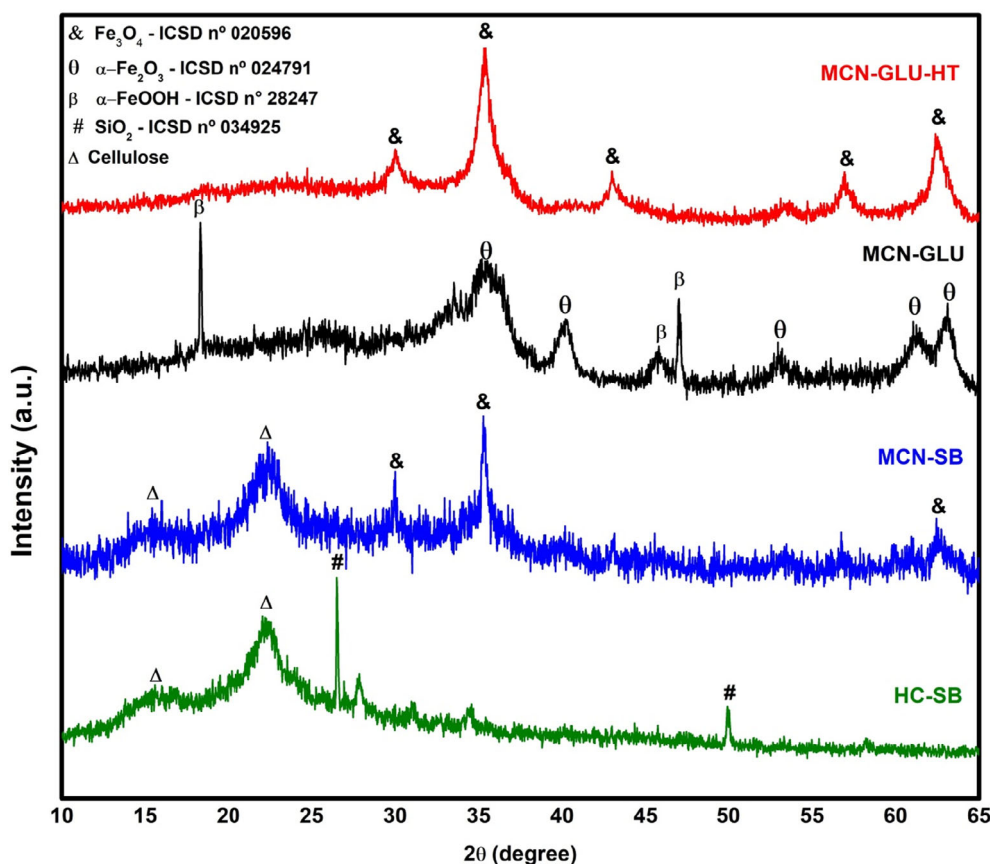


Figure 2. XRD patterns for HC-SB, MCN-SB, MCN-GLU and MCN-GLU-HT, showing the identification of inorganic phases. Source File: ORIGIN PRO 8.5.

cubic symmetry and space group $Fd\bar{3}m$ with lattice parameters $a = 8.3771 \text{ \AA}$ and $a = 8.3767 \text{ \AA}$, respectively. Such a refinement revealed goodness-of-fit (S_{GOF}) between the parameters with S_{GOF} next to one. These results indicate a large amount of superparamagnetic nanoparticles (SPM) in the nanocomposites, where the average particle size of MCN-GLU-HT (7.5 nm) and of MCN-SB (9.5 nm) were smaller than the critical superparamagnetic diameter of magnetite (20.0 nm).³⁵

The functional groups on the surface of the as-prepared nanocomposites (MCN-GLU, MCN-GLU-HT and MCN-SB) and SB were identified using FTIR analysis (Fig. 3). In the FTIR spectrum of SB it is possible to see a broad and intense band between 3600–3000 cm^{-1} , assigned to stretching vibrations of O–H bonding from cellulose, hemicellulose and lignin.³⁶ Deformation of aliphatic C–H bonding from methylene groups (CH_2) of chains attached to cellulose and lignin residues,³⁷ also can be verified as weak bands at 2919 and 2850 cm^{-1} . However, MCN-SB and MCN-GLU show low-intensity bands in these regions, which denotes that dehydration reactions occurred to a great extent during the HTC process.

The shoulder at 1697 cm^{-1} confirms the presence of C=O groups (–COOR or COOH) on the surface of MCN-SB, MCN-GLU and MCN-GLU-HT, whereas the more intense band at 1584 cm^{-1} is known as stretching vibration of skeletal C=C in aromatic rings,¹² suggesting an increase of aromatic domains in these materials, but particularly in the case of MCN-GLU-HT, corroborating the higher temperature of degradation as observed in TGA analysis. The intense band between 1126 and 922 cm^{-1} , centred on 1032 cm^{-1} in the FTIR spectrum of SB, corresponds to C–O–C stretching vibration of the cellulose chain and also to C–O and C–OH stretching vibration of alcohol groups.¹⁶ As can be seen, this band is also present in the spectrum for MCN-SB, suggesting that part of the cellulose was not degraded during HTC of SB at 250 °C. Strong bands at 561 and 438 cm^{-1} were observed in the spectra of MCN-SB and MCN-GLU, corresponding to the Fe–O stretching vibration, further confirming the incorporation of iron oxides in the carbonaceous matrix,^{16,38} corroborating the TGA, EDS and TEM results (Figs 1 and 4).

Thus, the FTIR technique allowed us to infer the main functional groups present on the surface of nanocomposites. The products from hydrothermal treatment (MCN-SB and MCN-GLU) showed a surface containing a wider range of functional groups, such as –OH, C–O, C=O and COOH groups. Regarding the sample that was thermally treated (MCN-GLU-HT), great loss of functional groups from its surface was verified, albeit presenting a more aromatic structure. It is important to highlight that the existence of a carbonaceous layer is of great importance to avoid the oxidation of iron oxide nanoparticles in the core of the material, as well as having a key role in providing adsorption sites for the material.

Textural and morphological evaluation of the nanocomposites

Details about the morphology of the magnetic nanocomposites (MCN-GLU-HT and MCN-SB) were obtained by SEM [Fig. 4(a) and (e)]. The SEM images of the nonmagnetic samples (HC-SB and MCN-GLU) are shown in the Supporting information [Fig. S1 (a) and (b)].

Figure 4(a) shows the SEM image of the MCN-GLU-HT sample revealing micrometric particles of spherical morphology characteristic of the hydrothermal carbonisation of glucose. It is already well-known that micrometric spherical particles are produced from HTC of carbohydrates.³⁹ The elemental mapping

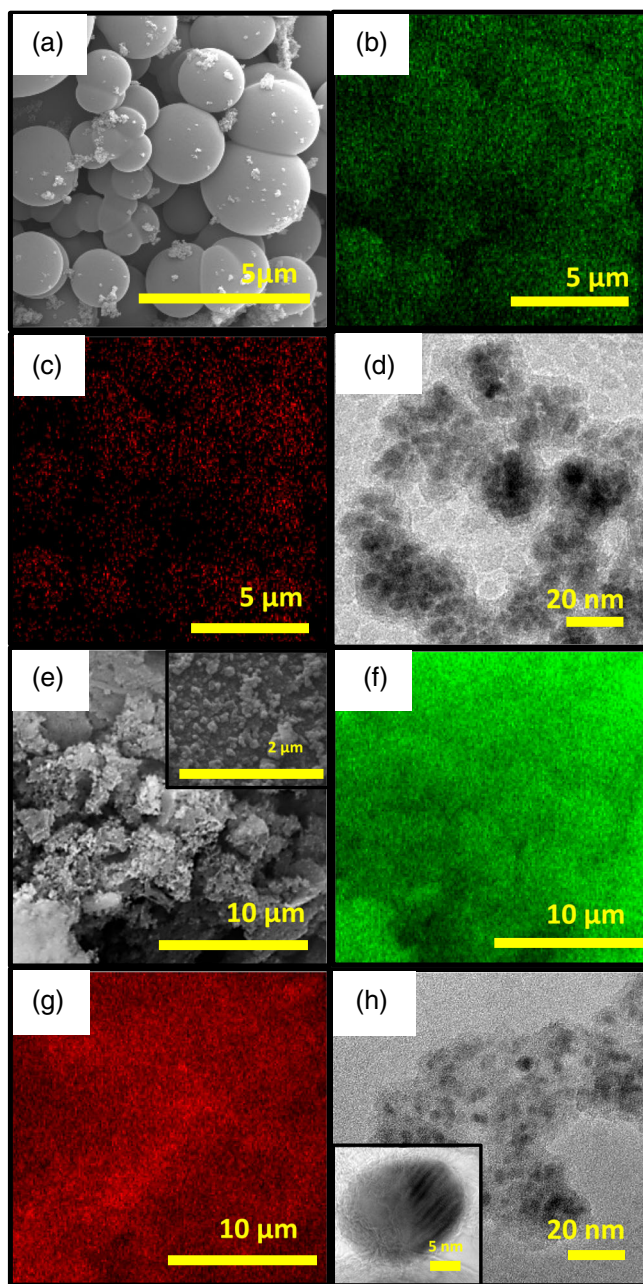


Figure 4. MCN-GLU-HT: (a) SEM image; elemental maps containing (b) carbon (green) and (c) iron distribution (red); (d) TEM image. MCN-SB: (e) SEM image with inset showing microspherical particles; (f) elemental maps containing carbon (green) and (g) iron distribution (red); and (h) TEM image with inset showing a typical oxide iron nanoparticle (average diameter 9.7 nm). Source File: Aztec (Oxford).

represented in Fig. 4(b) and (c) shows a uniform distribution of iron throughout the carbonaceous matrix, suggesting an efficiency of the synthesis method in the encapsulation of the inorganic phase in the carbonaceous matrix. It is possible to observe some adhered nanoparticles on the surface of the microparticles in the SEM images. The TEM image [Fig. 4(d)] shows nanoparticles embedded in the carbonaceous matrix of the MCN-GLU-HT samples, revealed by the presence of dark spots with light external regions, thus configuring the encapsulation of Fe_3O_4 nanoparticles, with an average diameter of 10 nm in this nanocomposite. The

effectiveness of the HTC method for production of C spheres embedded with iron oxide nanoparticles from glucose and metallic salts has been reported previously in the literature.^{9,25,40} However, the system cannot be defined as a core-shell, given that we do not have a single particle (core) coated with C (shell) but instead an agglomerate of particles (Fe_3O_4) covered by layers of C.

Figure 4(e) shows a SEM image of the MCN-SB composite where it is possible to observe particles with the morphology of plates containing irregular agglomerates made up of nanoparticles on the surface. The morphologies described here are similar to those observed by other authors who prepared samples of magnetic C using iron(III) nitrate and cellulose, but using the pyrolysis method.^{10,41} The similarities between the morphologies observed for the MCN-SB and HC-SB samples [Fig. S1(a)] and the discrepancies between MCN-SB in relation to the MCN-GLU [Fig. S1(b)] and MCN-GLU-HT samples [Fig. 4(a)] probably are a result of the partial carbonisation suffered by SB at 250 °C during HTC. In this process, the biomass fractions that have greater thermal stability (cellulose and lignin) still remain as residues in the hydrothermal C composition,²⁸ which is corroborated by the XRD data, which indicated the presence of an amorphous phase in the material, associated with cellulose. The EDS spectra [Fig. 4(f) and (g)] indicated the presence of the basic elements for the formation of the MCN-SB composite, which are Fe and C. The TEM image of MCN-SB [Fig. 4(h)] shows nanoparticles with iron oxide cores coated with C layers with average diameters close to 9.7 nm, resembling those obtained for the MCN-GLU-HT composite. The TEM images corroborate to the results obtained from the Rietveld refinements of the XRD patterns.

The textural properties of carbonaceous nanomaterials were investigated using the N_2 adsorption-desorption isotherms (Fig. 5). It can be seen that MCN-GLU-HT shows the type IV isotherm, characteristic of mesoporous solids, as defined by IUPAC classification,⁴² with higher N_2 adsorption than MCN-SB. This result could be due to the thermal treatment that promoted

chemical reactions producing gases such as $\text{CO}/\text{CO}_2/\text{CH}_4$ and leading to development of porosity.²⁵ However, MCN-SB is a material that was just carbonised, showing a type III isotherm. This profile is typical of nonporous solid, characteristic of carbonaceous products prepared via hydrothermal carbonisation,⁹ where in this case N_2 molecules stay close to more favourable sites rather than diffusing into the material. In addition, as reported in Table 2, the MCN-GLU-HT sample showed higher specific surface area ($90 \text{ m}^2 \text{ g}^{-1}$) than MCN-SB ($53 \text{ m}^2 \text{ g}^{-1}$), a fact also consistent with the higher N_2 volume adsorbed on MCN-GLU-HT (Fig. 5).

The measure of the zeta potential of a sample is essential to check the surface charge of the particles when dispersed in aqueous solution, because this property can influence the interaction between adsorbent and adsorbate.^{43,44} From Table 2, it can be observed that both produced MCN have negatively charged surfaces, of -34.8 mV for MCN-GLU-HT and -34.1 mV for MCN-SB at pH of 5.0. These results suggest the presence of acidic groups on the surface of these materials such as phenyl, carbonyl and carboxyl, as identified in FTIR analysis (Fig. 3). According to what has been discussed in the literature about the interaction between Cr (VI) and magnetic nanocomposites, some active groups such as unsaturated $\text{C}=\text{C}$ double bonds and hydroxyl $\text{C}-\text{OH}$ can act as electron donors, contributing for the reduction of Cr (VI) to Cr (III).¹⁶ Corroborating with this statement, both species were found on the surface of these materials by XPS analysis, which suggests that Cr (VI) removal process takes place through adsorption-reduction.^{11,16} In this way, the positive specie [Cr (III)] can interact easily with a material that has a negatively charged surface, thus favouring Cr(VI) removal from the solution.

Magnetic measurement and identification of the iron oxide phases

The magnetic properties of the nanocomposites were evaluated by VSM measurements of at room temperature (Fig. 6). The MCN-GLU sample does not present a hysteresis curve, possibly

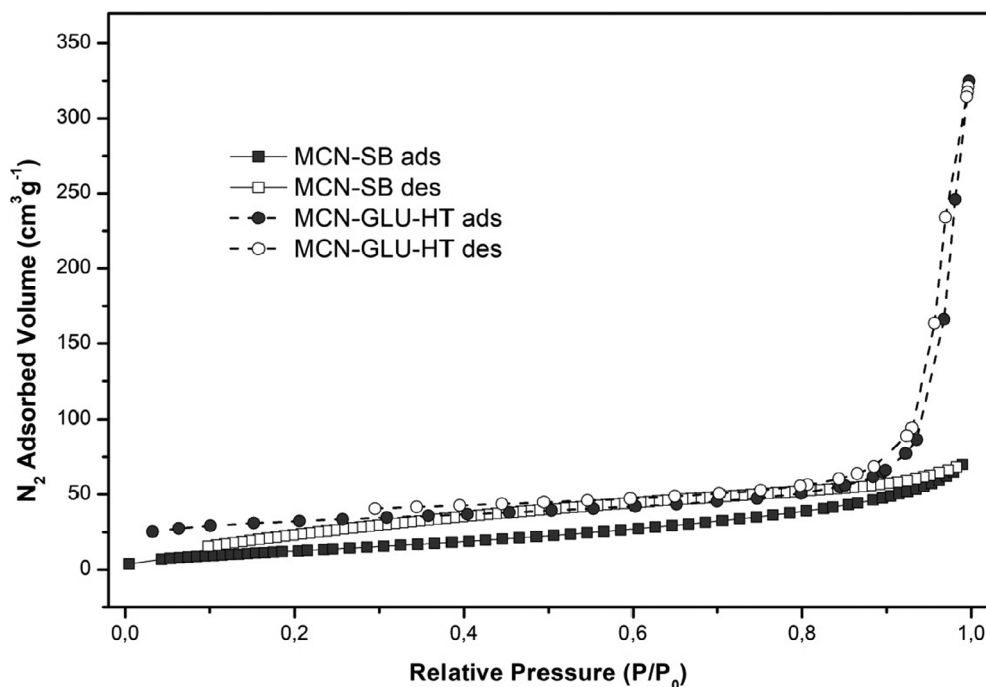


Figure 5. N_2 adsorption-desorption isotherms obtained for MCN-SB and MCN-GLU-HT at $-196 \text{ }^\circ\text{C}$. Source File: ORIGIN PRO 8.5.

Table 2. Textural properties obtained from N₂ adsorption–desorption isotherms and zeta potential measurements for the magnetic nanocomposites

Samples	S_{BET} (m ² g ⁻¹) ^a	Total pore volume (cm ³ g ⁻¹) ^b	Zeta potential (mV)
MCN-SB	53	0.108	-34.1
MCN-GLU-HT	90	0.447	-34.8

^a Specific surface area was calculated by BET method ($p/p_0 = 0.99$).

^b Calculated by BJH method.

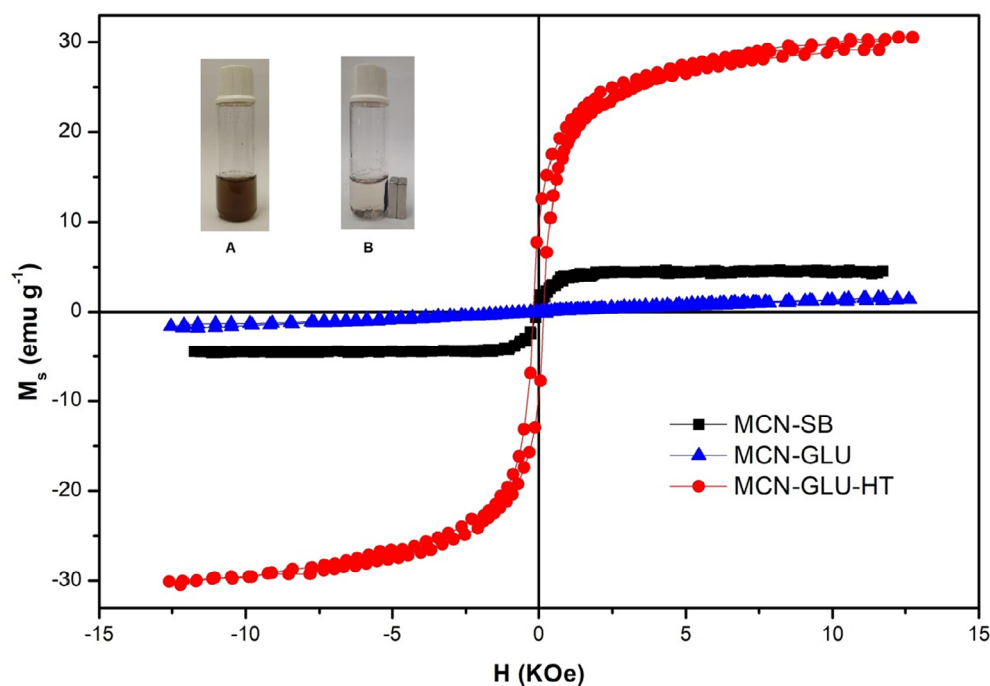


Figure 6. Magnetisation curves of the prepared MCNs at room temperature. Insets show MCN-SB dispersed in ultrapure water (a) in the absence and (b) in the presence of a magnetic field. Source File: ORIGIN PRO 8.5.

due to the diamagnetic contribution of the C layers, in addition to the paramagnetic behaviour of the hematite and the antiferromagnetic properties of the goethite.³³ As a result, linear magnetisation with the applied magnetic field is obtained. The magnetisation curves of the MCN-SB and MCN-GLU-HT nanocomposites show narrow hysteresis, with low values of coercive fields (Fig. 6). In the sample of MCN-GLU-HT, a maximum magnetisation of 30.5 emu g⁻¹ was obtained, without saturation in magnetisation. This is the result of a strong contribution made by superparamagnetic particles, as the critical SPM size (d_{SPM}) for magnetite is ≈ 10 nm. Therefore, most of the particles in this sample are below this size, as shown by the Rietveld refinement result. However, due to particle size distribution, there are magnetic particles in the MCN-GLU-HT sample that are larger than d_{SPM} , where they are in the blocked magnetic state, contributing to the presence of a coercive field.

In the MCN-SB sample, the nanoparticles are in the magnetically stable single-domain, with little contribution from the SPM particles, and here we observed a sample saturation in a low external field ($H_{\text{sat}} = 2.5$ kOe). However, the saturation magnetisation value ($M_s = 5.0$ emu g⁻¹) was lower due to the large amount of nonmagnetic hydrothermal C present in this composite. It also is worth commenting that magnetite has high magnetic susceptibility, meaning a quick response to an external magnetic field, an

important characteristic for adsorption applications where the solid–liquid separation from the aqueous medium can be carried out magnetically.

These results show that hydrothermal synthesis was able to produce magnetic iron phase nanoparticles in the presence of SB, which remained ingrained in the carbonaceous matrix of nanocomposites, as confirmed by EDS and XRD analysis [Figs 2 and 4 (g)]. Meanwhile, in the case of glucose, it was necessary to submit the hydrothermal material (MCN-GLU) to thermal treatment, so that magnetisation could be achieved.

Electronic paramagnetic resonance spectroscopy, a very sensitive tool for the study of iron oxide nanoparticles,⁴⁵ was carried out at room temperature to optimise the distinction of the magnetic phases present in the MCNs. Figure S2(a),(b) shows asymmetric resonance lines for the MCN-GLU-HT and MCN-SB samples, probably due to more than one pattern of magnetic behaviour. XRD results have already shown the predominance of the Fe₃O₄ crystalline phase and the magnetic measurements showed magnetic properties in nanoparticles with a magnetic single domain. Therefore, the EPR spectra obtained must result from more than one magnetic contribution.

In order to interpret the EPR spectra, it was necessary to perform a deconvolution process; for this, Lorentzian functions were used

Table 3. Parameters of EPR spectra obtained by deconvolution with Lorentzian functions

Sample	Lorentzian	ΔH_{pp} (G)	H_r (G)	g factor	% SPM	%BP
MCN-SB	1	1540	2885	2.40	—	70
	2	1010	3356	1.94	30	—
MCN-GLU-HT	1	1330	3016	2.30	—	13
	2	936	3400	2.04	87	—

ΔH_{pp} , peak-to-peak line width; H_r , resonance field; g , gyromagnetic factor; SPM, superparamagnetic particles; BP, blocked particles.

to adjust the spectra of these samples. Table 3 shows these results and the variation of the magnetic field referring to the peak-to-peak line width (ΔH_{pp}), the resonance field (H_r), the g factor, and the percentage of superparamagnetic and blocked particles. For noninteracting SPM particles of magnetite, a factor of $g = 2$ is expected, and therefore, for a microwave frequency $\nu = 9.7$ GHz, the expected value of resonance field H_{res} is 3450 G ($H_{res} = h\nu/\mu_B$, where h is the Planck constant and μ_B is the Bohr magneton).

In the MCN-GLU-HT sample, $H_{res} = 3400$ G, a factor $g = 2.04$ and a line width from peak to peak $\Delta H_{pp} = 936$ G were obtained. The values of H_{res} and g obtained are very close to that expected for superparamagnetic particles of magnetite. The high ΔH_{pp} value indicated a strong magnetic interaction between these SPM particles, which resulted in the $H_c = 170$ Oe value on the $M \times H$ curve. The obtained parameters also show the predominance of SPM particles in this sample, 87%.

In the MCN-SB sample, the obtained parameters with the adjustment for Lorentzian 1 were $H_{res} = 2885$ G, $g = 2.40$ and $\Delta H_{pp} = 1540$ G. The value particle size of 9.5 nm (obtained from Rietveld Refinement) in this MCN is smaller than the SPM diameter for Fe_3O_4 particles. When the particles are in a magnetically blocked state, the resonance field decreases and the g value increases, mainly due to magnetocrystalline anisotropy. The resonance field predicted for single-domain spherical particles with cubic structure is $H_{res} = h\nu/\mu_B g - 2|K_1|/M_s$, where K_1 is the magnetocrystalline anisotropy constant and M_s is the saturation magnetisation.⁴⁶ From this equation, the value of $|K_1| = 13 \times 10^4$ erg cm^{-3} was calculated, using $M_s = 460$ emu cm^{-3} for bulk magnetite.⁴⁷ The obtained value of the anisotropy constant, for room temperature, agreed with the value predicted in the literature for magnetite with cubic symmetry.⁴⁸ In this MCN-SB sample, the magnetically stable (blocked) single-domain particles predominate, at $\approx 70\%$, which is different to the MCN-GLU-HT sample, where there is a prevalence of SPM particles. The EPR result for the MCN-SB sample is characteristic for the non-uniform particle size distribution, corroborating with the VSM measurement (Fig. 6).

Characterization of the magnetic nanocomposites as adsorbents

The nanocomposites that exhibited magnetic behaviour (MCN-SB and MCN-GLU-HT) were employed in batch adsorption studies, aiming to characterise these materials as adsorbent. For this study, Cr (VI) was chosen as adsorbate, because recently some works with magnetic composites^{10,11,15,16} have used this chemical species to evaluate the adsorbent property of these materials. Here, the batch experiments included a study of the contact time of each material with Cr (VI) solution and a study of the effect of the Cr (VI) concentration used. The effect of contact time on chromium adsorption was estimated by using a 30 mL solution

containing 1000 $\mu g L^{-1}$ Cr (VI), with an initial pH of 5.0, adsorbent dosage of 0.5 $g L^{-1}$ and contact time ranging from 1 to 24 h.

The Cr (VI) removal profiles are very similar for both materials, where a fast initial Cr (VI) removal occurred, as can be seen in Figs 7 and S3, which was most prominently for MCN-GLU-HT (35%). Then, the Cr (VI) removal slowed down until 10 h, when a Cr (VI) removal of $\approx 60\%$ and 21%, corresponding to the values of 1024 and 388 $\mu g g^{-1}$, respectively, were achieved for MCN-GLU-HT and MCN-SB. Between 10 and 24 h, additional Cr (VI) removals of 10% and 17% were obtained (respectively) for MCN-GLU-HT and MCN-SB. So, after 24 h, the Cr (VI) removal reached ≈ 738 $\mu g g^{-1}$ for MCN-SB and 1199 $\mu g g^{-1}$ for MCN-GLU-HT, corresponding to Cr (VI) removal of 39% and 70%, respectively (Fig. S3).

The higher Cr (VI) removal values obtained for MCN-GLU-HT resulted from the higher surface area shown by this magnetic nanocomposite in relation to MCN-SB (Table 2). In the same way, the surface area had a strong effect on the Cr (VI) removal performance of an MCN produced from cellulose, when conducted in neutral solution, as more adsorption sites were available for interacting with Cr (VI) ions.¹⁰ In this case, the sample that exhibited the highest surface area (247.14 $m^2 g^{-1}$), also showed the highest Cr (VI) removal value (22.8 $mg g^{-1}$), whereas the opposite was observed for those with the smallest surface area (82.94 $m^2 g^{-1}$), that showed the lowest Cr (VI) removal value (10.2 $mg g^{-1}$).

In order to evaluate the experimental kinetic data obtained from Cr (VI) batch adsorption, three kinetic models were chosen: PFO, PSO and Elovich. The nonlinear equations of these kinetic models are given in Table S1. The obtained kinetic parameters values are shown in Table 4. The PFO model describes that the adsorption rate is dependent only on the solid/liquid interface, whereas the PSO model assumes that the adsorption rate is mass-dependent and that the chemical sorption is a rate-limiting step.⁴⁹ The Elovich model, in turn, is an empirical equation that also takes into account the contribution of desorption.²⁴

According to the correlation coefficients (R^2) obtained from the kinetic data adjustment, the PSO model (0.7574 and 0.9938) describes the kinetic results more adequately than the PFO model (0.7445 and 0.8747) or Elovich model (0.7533 and 0.9904) for MCN-SB and MCN-GLU-HT, respectively [Table 4; Fig. S4(a) and (b)]. In addition, experimental q_t values obtained after 24 h of kinetics (MCN-SB: 737.86 $\mu g g^{-1}$, MCN-GLU-HT: 1199.36 $\mu g g^{-1}$) were closer to the calculated q_e values obtained using the PSO model (MCN-SB: 665 $\mu g g^{-1}$, MCN-GLU-HT: 1180 $\mu g g^{-1}$), than those obtained based on the PFO model (MCN-SB: 479 $\mu g g^{-1}$, MCN-GLU-HT: 817 $\mu g g^{-1}$), which implies that chemical sorption might play a key role in the process and is likely to be a rate-limiting step of the removal of Cr (VI) from water for both MCNs. Cai *et al.* (2019) reported that Cr (VI) adsorption rates on amino-

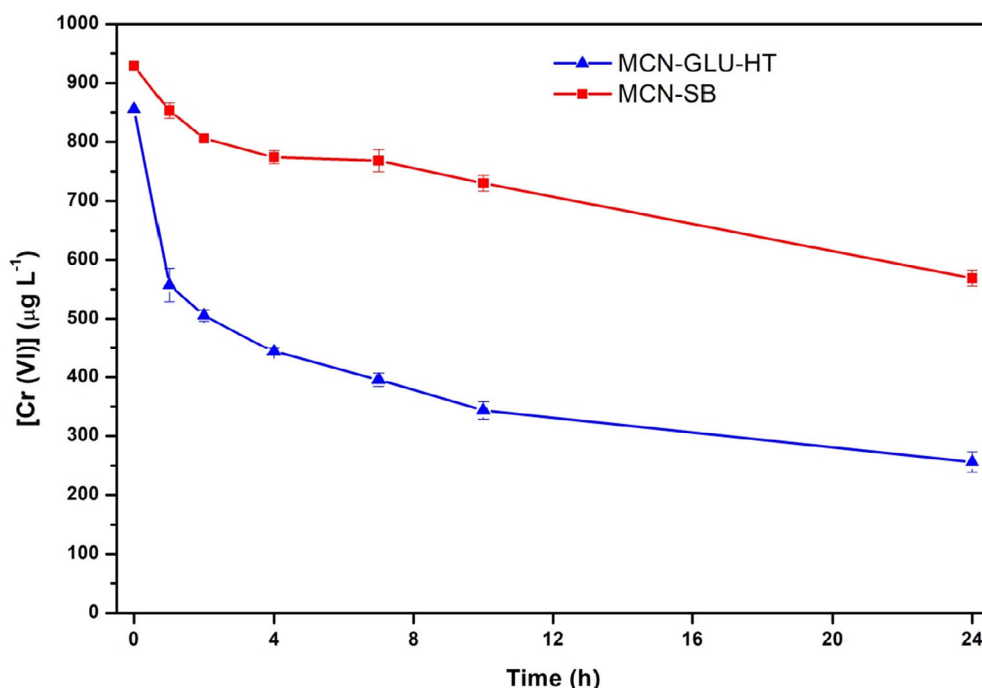


Figure 7. Cr (VI) amount in solution with increasing contact time using MCN-SB and MCN-GLU-HT. Adsorption conditions: [Cr (VI)]: 1000 $\mu\text{g L}^{-1}$; times: 1, 2, 4, 7, 10 and 24 h; pH 5.0; adsorbent dosage 0.5 mg L^{-1} ; volume 30 mL ($n = 3$, mean values). Source File: ORIGIN PRO 8.5.

Table 4. Kinetic parameters calculated using PFO, PSO and Elovich models for Cr (VI) removal using MCN-SB and MCN-GLU-HT

Model	Sample	Kinetic parameters		
Experimental data			$q_{t,24}^a$ ($\mu\text{g g}^{-1}$)	
	MCN-SB	738		
	MCN-GLU-HT	1199		
PFO		k_1 (min^{-1})	q_e ($\mu\text{g g}^{-1}$)	R^2
	MCN-SB	0.0608	479	0.7445
	MCN-GLU-HT	0.1636	817	0.8747
PSO		k_2 ($\text{g mg}^{-1} \text{min}^{-1}$)	q_e ($\mu\text{g g}^{-1}$)	R^2
	MCN-SB	1.36×10^{-4}	665	0.7574
	MCN-GLU-HT	4.04×10^{-4}	1180	0.9938
Elovich		α ($\text{mg g}^{-1} \text{h}^{-1}$)	β (g mg^{-1})	R^2
	MCN-SB	0.3099	6.31	0.7533
	MCN-GLU-HT	3.8631	5.23	0.9904

^a q_t after 24 h.

functionalised magnetic biochar obtained from peanut hulls also was controlled by chemical interactions, in which the $\gamma\text{-Fe}_2\text{O}_3$ phase over an adsorbent surface hindered Cr (VI) ion diffusion to the biochar, thereby contributing to a slower adsorption rate (k_2 : $0.20 \times 10^{-3} \text{ g mg}^{-1} \text{ min}^{-1}$) compared with nonmagnetic biochar (k_2 : $1.13 \times 10^{-3} \text{ g mg}^{-1} \text{ min}^{-1}$). The chemical interaction can take place by sharing or exchanging electrons between some active groups (C=C and C-OH) from the magnetic C adsorbent surface and CrO_4^- and $\text{Cr}_2\text{O}_7^{2-}$ ions present in solution.¹⁶ Also according to this study, $\gamma\text{-Fe}_2\text{O}_3$ contributed to Cr (VI) removal, through the mechanism of electrostatic interaction, because the iron oxide has a positive charge at low pH.

The effect of initial Cr (VI) concentration (C_0) on the Cr (VI) uptake by magnetic nanocomposites also was analysed, using

initial Cr (VI) concentrations ranging from 300 to 1100 $\mu\text{g L}^{-1}$, which remained in contact with 0.5 g L^{-1} of each material over a period of 10 h. From Fig. 8, we see that, as C_0 concentration increases, there is a steep increase in Cr (VI) uptake, which can be attributed to a greater mass transfer driving force at higher C_0 ,⁵⁰ reaching 939 $\mu\text{g g}^{-1}$ for MCN-GLU-HT and 768 $\mu\text{g g}^{-1}$ for MCN-SB in the higher Cr (VI) concentration used. These adsorption capacities are of the same order as those reported for other magnetic carbonaceous materials.^{15,51} The adsorption limit could be associated to a limited number of adsorption sites on nanocomposite surfaces, reaching saturation and limiting the Cr (VI) removal by these materials.

In order to explore the Cr (VI) adsorption behaviour for each adsorbent, we used two nonlinear isotherm models (Langmuir

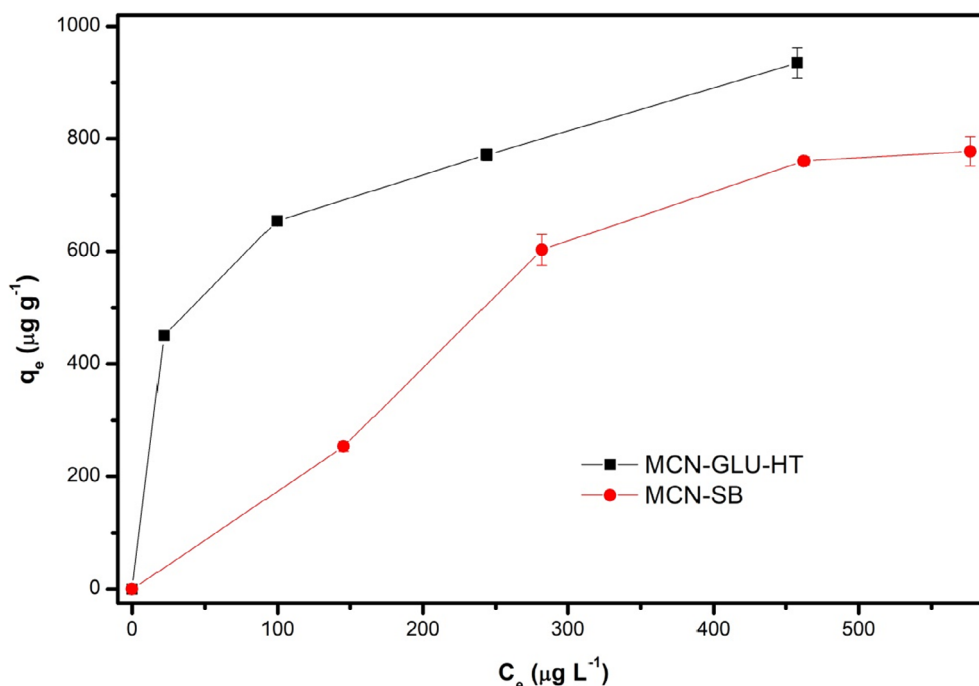


Figure 8. Adsorption isotherms using MCN-SB and MCN-GLU-HT as adsorbents. Adsorption conditions: [Cr (VI)]: 300, 500, 700, 900 and 1100 $\mu\text{g L}^{-1}$; adsorbent dosage 0.5 g L^{-1} ; volume 30 mL; pH 5.0; equilibrium time 10 h ($n = 3$, mean values). Source File: ORIGIN PRO 8.5.

Table 5. Isotherm parameters obtained from Cr (VI) removal experimental data using MCN-SB and MCN-SB-HT adjusted to Langmuir and Freundlich models

Model	Sample	Isotherm parameters		
Langmuir	MCN-SB	Q_{max} (mg g^{-1})	K_L (L g^{-1})	R^2
	MCN-GLU-HT	n.a.	n.a.	0.3887
Freundlich	MCN-SB	0.92	0.026	0.9488
	MCN-GLU-HT	K_F (mg g^{-1})(mg L^{-1}) $^{-1/n}$	n_F	R^2
	MCN-SB	1.94	1.21	0.8909
	MCN-GLU-HT	10.81	4.78	0.9006

n.a., not applicable.

and Freundlich) to fit the experimental data of equilibrium adsorption [Fig. S5(a) and (b)]. The nonlinear equations of these isotherm models are provided in Table S2. The Langmuir model assumes that the adsorbent contains definite identical binding sites, homogeneously distributed on the surface, where the uptake of adsorbate is controlled by chemical adsorption, limited by a monolayer coverage.⁵² The Freundlich model, however, is more suitable for multilayer adsorption process and heterogeneous surfaces, with nonuniform distribution of adsorption energy.¹⁶

The Langmuir model ($R^2 = 0.9488$) was more suitable for the assessment of Cr (VI) adsorption on MCN-GLU-HT than the Freundlich model ($R^2 = 0.9006$), as indicated in Table 5 and Fig. S5 (a) and (b). However, the Cr (VI) adsorption on MCN-SB seemingly was better explained by the Freundlich ($R^2 = 0.8909$) rather than the Langmuir model ($R^2 = 0.3887$). This difference in behaviour patterns could be related to the higher heterogeneity of the MCN-SB surface, due to fragments of cellulose and lignin that remained in the structure even after hydrothermal carbonisation,

as indicated by higher carbonaceous content and abundance of functional groups, as shown by TGA and FTIR (Table 1, Fig. 3).

According to the Langmuir model, MCN-GLU-HT showed a maximum Cr (VI) removal capacity (Q_{max}) of 0.92 mg g^{-1} at room temperature. Turning now to MCN-SB, it was not possible to determine the maximum removal capacity, as the Freundlich model does not provide that kind of information. However, this model has two parameters, K_F and n_F , which are, in turn, indirectly related to adsorption capacity and intensity, incorporating all factors affecting the adsorption process.⁵³ According to this model, the higher the K_F values, the greater the adsorption capacity. Moreover, it is possible to establish if the adsorption process is favourable ($1/n_F < 1.0$) or not ($1/n_F > 1.0$). For MCN-SB, it was shown that Cr (VI) adsorption process is favourable ($1/n_F = 0.83$), indicating a greater affinity of Cr (VI) with MCN-SB.

The chromium removal capacities obtained in this study were compared with those obtained with other magnetic nanocomposites,^{10,11,15,16,19,54,55,56} as can be seen in Table 6. Magnetic Cs prepared via pyrolysis have high removal capacities, mainly due to

Table 6. Comparison of Cr (VI) amount removed in kinetic experiments using magnetic Cs and its proposed removal mechanisms

Magnetic adsorbent	Cr (VI) amount removed (mg g ⁻¹) and experimental conditions	Proposed mechanism of Cr (VI) removal	References
Magnetic C from cellulose	278.8 {[Cr(VI)]: 2000 mg L ⁻¹ , t = 30 min, dose 2.5 g L ⁻¹ , pH 2.0}	Reduction	10
Melamine-derived N-doped magnetic C	7.5 {[Cr(VI)] 40 mg L ⁻¹ , t = 2.5 min, dose 2.5 g L ⁻¹ , pH 7.0}	Reduction and Adsorption	11
Activated sludge-derived magnetic C	203.0 {[Cr(VI)] 1000 mg L ⁻¹ , t = 10 min, dose 1.0 g L ⁻¹ , pH 3.0}	Reduction	15
Peanut hull-derived magnetic biochar	97.9 {[Cr(VI)] 100 mg L ⁻¹ , t = 24 h, dose 1.0 g L ⁻¹ , pH 2.0}	Redox reaction and electrostatic attraction	16
Magnetic activated C from termite faeces	49.0 {[Cr(VI)] 125 mg L ⁻¹ , t = 4 h, dose 2.5 g L ⁻¹ , pH 4.0}	Adsorption–reduction process	19
Nanomodified SB	0.27 {[Cr(VI)] 100 mg L ⁻¹ , t = 2.5 h, dose 10.0 g L ⁻¹ , pH 1.0}	Not determined	55
Fe ₃ O ₄ /GO ^a	6.0 {[Cr(VI)] 5 mg L ⁻¹ , t = 1 h, dose 0.15 g L ⁻¹ , pH 2.0}	n.d.	56
SB-derived magnetic C (MCN-SB)	0.74 {[Cr(VI)] 1 mg L ⁻¹ , t = 24 h, dose 0.5 g L ⁻¹ , pH 5.0}	n.d.	This study
Glucose-derived magnetic C (MCN-GLU-HT)	1.20 {[Cr(VI)] 1 mg L ⁻¹ , t = 24 h, dose 0.5 g L ⁻¹ , pH 5.0}	n.d.	This study

Data obtained from the literature.
^a GO, graphene oxide.^a n.d., not determined

the large surface area, as reported for magnetic Cs from cellulose¹⁰ ($q_e = 278.8 \text{ mg g}^{-1}$, $S_{\text{BET}} = 136.3 \text{ m}^2 \text{ g}^{-1}$), activated-sludge¹⁵ ($q_e = 203.0 \text{ mg g}^{-1}$, $S_{\text{BET}} = 114.2 \text{ m}^2 \text{ g}^{-1}$), termite feces¹⁹ ($q_e = 49.0 \text{ mg g}^{-1}$, $S_{\text{BET}} = 699.0 \text{ m}^2 \text{ g}^{-1}$) and melamine¹¹ ($q_e = 7.5 \text{ mg g}^{-1}$, $S_{\text{BET}} = 56.2 \text{ m}^2 \text{ g}^{-1}$). Nevertheless, the pH of the solution also is an important factor in chromium removal, because magnetic Cs are able to remove more Cr (VI) under acidic conditions than neutral conditions, as observed in several previous works.^{10,11,15}

In fact, when the removal of Cr (VI) by a magnetic C obtained by hydrothermal method, from peanut hulls¹⁶ (MPC-HDA), is compared with the results obtained in this work for magnetic Cs produced by the same method from SB (MCN-SB) or of glucose (MCN-GLU-HT), it was verified that despite the similar values of surface area, the removal occurred more significantly for MPC-HDA, applied at pH 2.0 ($q_e = 97.9 \text{ mg g}^{-1}$, $S_{\text{BET}} = 62.4 \text{ m}^2 \text{ g}^{-1}$) than for MCN-SB ($q_e = 0.7 \text{ mg g}^{-1}$, $S_{\text{BET}} = 53.0 \text{ m}^2 \text{ g}^{-1}$) or MCN-GLU-HT ($q_e = 1.2 \text{ mg g}^{-1}$; $S_{\text{BET}} = 90.0 \text{ m}^2 \text{ g}^{-1}$), both applied at pH 5.0. However, magnetic Cs obtained from the chemical coprecipitation method have Cr (VI) removal capacities closer to the materials produced in this work, such as Fe₃O₄-nanomodified SB⁵⁶ (0.3 mg g^{-1}) and magnetic graphene oxide⁵⁵ (6.0 mg g^{-1}), even though the material was applied in acidic media, respectively at pH 1.0 and 2.0.

CONCLUSION

In this work, HTC was used to produce MCNs appropriate for Cr (VI) removal, using SB as a source of C (MCN-SB). This material showed good magnetic response, due to the magnetite nanoparticles incorporated by the carbonaceous matrix of the nanocomposite. In addition, its carbonaceous structure has an abundance of oxygenated functional groups. However, the use of glucose in the HTC instead of SB, resulted in a nonmagnetic nanocomposite

(MCN-GLU), requiring heat treatment to achieve magnetisation (MCN-GLU-HT). EPR revealed that the majority of magnetite nanoparticles in the MCN-GLU-HT are superparamagnetic, whereas for MCN-SB, most of these nanoparticles are in the magnetically blocked state which, along with the higher iron content of MCN-GLU-HT, is responsible for its higher saturation magnetisation. Batch adsorption experiments showed that MCN-GLU-HT achieved a greater Cr (VI) removal after 24 h ($q_{t,24} = 1199 \mu\text{g g}^{-1}$) than MCN-SB ($q_{t,24} = 738 \mu\text{g g}^{-1}$), owing to its mesoporous surface and higher specific surface area ($S_{\text{BET}} = 90.1 \text{ m}^2 \text{ g}^{-1}$) when compared to MCN-SB, which has a nonporous surface and a S_{BET} of $52.6 \text{ m}^2 \text{ g}^{-1}$. The kinetic data of the adsorption fitted well with PSO kinetics for both MCNs, suggesting the contribution of chemical sorption in the process. The adsorption isotherm fitted better with the Langmuir model for MCN-GLU-HT, whereas the Freundlich model was more appropriate to describe this process for MCN-SB, owing to its heterogeneity. Therefore, findings suggest that is possible to use SB as a resource for obtain a new magnetic carbonaceous adsorbent for Cr (VI) removal, using a mild one-step hydrothermal method, which ensures greater simplicity and efficiency in the use of biomass for the production of these nanocomposites.

ACKNOWLEDGEMENTS

The authors are grateful to Central Analítica – UFC/CT–INFRA/MCTI–SISNANO/Pro-Equipamentos CAPES for providing the scanning electron microscopes, to Centro de Ciências e Tecnologia de Materiais (CCTM/IPEN/USP) for the transmission electron microscopy, to Laboratório de Sucroquímica e Química Analítica – UNESP/IBILCE for providing the infrared spectrometer and to Centro de Síntese e Análise de Materiais Avançados – CSAMA/UERN for providing the VSM and EPR analysis. The authors appreciate the financial support and scholarship from the São Paulo Research

Foundation-FAPESP (grants nos. 2005/51242-8, 2011/00574-1, 2012/23066-4, 2013/21776-7, 2014/10368-8, 2014/22400-3, 2015/22954-1, 2017/13230-5, 2017/26718-6, 2018/15733-7 and 2021/09126-3) and to University of São Paulo State (Recurso Ofício n° 348/2021-PROPG/SC) for assist in the cost of English proofreading. M.J.L. and F.H.S. gratefully acknowledges the doctoral scholarship received from CAPES-DS and to B.B.F. for the photos of the magnetic separation. M.C.B. acknowledges support from National Council for Scientific and Technological Development-CNPq (grant nos. 445487/2014-3 and 307925/2012-9). O.P.F. acknowledges support from the Cearense Foundation for the Support of Scientific and Technology Development (Fundação Cearense de Apoio ao Desenvolvimento Científico e Tecnológico —FUNCAP) (grant nos. PRONEX PR2-0101-00006.01.00/15 and 'Design Racional de Nanomateriais e Aplicações em Remediação Ambiental, Agricultura e Saúde') and also to CNPq through Grant 313637/2019-9 (CNPq DT 29/2019).

SUPPORTING INFORMATION

Supporting information may be found in the online version of this article.

REFERENCES

- Vidal F, Produção E Mercado De Etanol. *Cad Setorial ETENE* **121**:1–10 (2020).
- Perrone OM, de Moretti MMS, Bordignon SE, de Pereira JC, da Silva R, Gomes E *et al.*, Improving cellulosic ethanol production using ozonolysis and acid as a sugarcane biomass pretreatment in mild conditions. *Bioresour Technol Rep* **13**:100628 (2021). <https://doi.org/10.1016/j.biteb.2021.100628>
- Inácio JG, de Ferreira MA, Silva RC, de Silva JL, de Oliveira JCV, dos Santos DC *et al.*, Sugarcane bagasse as exclusive roughage for dairy heifers. *R Bras Zootec* **46**:80–84 (2017). <https://doi.org/10.1590/S1806-92902017000100012>.
- Zhong G, Huang J, Yao Z, Luo B, Li K, Xu S *et al.*, Intrinsic acid resistance and high removal performance from the incorporation of nickel nanoparticles into nitrogen doped tubular carbons for environmental remediation. *J Colloid Interface Sci* **566**:46–59 (2020). <https://doi.org/10.1016/j.jcis.2020.01.055>.
- Yan Q, Wan C, Liu J, Gao J, Yu F, Zhang J *et al.*, Iron nanoparticles in situ encapsulated in biochar-based carbon as an effective catalyst for the conversion of biomass-derived syngas to liquid hydrocarbons. *Green Chem* **15**:1631–1640 (2013). <https://doi.org/10.1039/C3GC37107G>.
- Quan H, Cheng B, Xiao Y and Lei S, One-pot synthesis of α -Fe₂O₃ nanoplates-reduced graphene oxide composites for supercapacitor application. *Chem Eng J* **286**:165–173 (2016). <https://doi.org/10.1016/j.cej.2015.10.068>.
- Dobson J, Gene therapy progress and prospects: magnetic nanoparticle-based gene delivery. *Gene Ther* **13**:283–287 (2006). <https://doi.org/10.1038/sj.gt.3302720>.
- Hiemstra T, Surface structure controlling nanoparticle behavior: magnetism of ferrihydrite, magnetite and maghemite. *Environ Sci Nano* **5**:752–764 (2018). <https://doi.org/10.1039/C7EN01060E>.
- Vieira LHS, Sabino CMS, Soares Júnior FH, Rocha JS, Castro MO, Alencar RS *et al.*, Strategic design of magnetic carbonaceous nanocomposites and its application as multifunctional adsorbent. *Carbon* **161**:758–771 (2020). <https://doi.org/10.1016/j.carbon.2020.01.089>.
- Qiu B, Wang Y, Sun D, Wang Q, Zhang X, Weeks BL *et al.*, Cr(VI) removal by magnetic carbon nanocomposites derived from cellulose at different carbonization temperatures. *J Mater Chem A* **3**:9817–9825 (2015). <https://doi.org/10.1039/C5TA01227A>.
- Cao Y, Huang J, Li Y, Qiu S, Liu J, Khasanov A *et al.*, One-pot melamine derived nitrogen doped magnetic carbon nano-adsorbents with enhanced chromium removal. *Carbon* **109**:640–649 (2016). <https://doi.org/10.1016/j.carbon.2016.08.035>.
- Feiqiang G, Xiaolei L, Xiaochen J, Xingmin Z, Chenglong G and Zhonghao R, Characteristics and toxic dye adsorption of magnetic activated carbon prepared from biomass waste by modified one-step synthesis. *Colloids Surf A Physicochem Eng Asp* **555**:43–54 (2018). <https://doi.org/10.1016/j.colsurfa.2018.06.061>.
- Rattanachueskul N, Saning A, Kaowphong S, Chumha N and Chuenchom L, Magnetic carbon composites with a hierarchical structure for adsorption of tetracycline, prepared from sugarcane bagasse via hydrothermal carbonization coupled with simple heat treatment process. *Bioresour Technol* **226**:164–172 (2017). <https://doi.org/10.1016/j.biortech.2016.12.024>.
- Khan MA, Alqadami AA, Wabaidur SM, Siddiqui MR, Jeon BH, Alshareef SA *et al.*, Oil industry waste based non-magnetic and magnetic hydrochar to sequester potentially toxic post-transition metal ions from water. *J Hazard Mater* **400**:123247 (2020). <https://doi.org/10.1016/j.jhazmat.2020.123247>.
- Gong K, Hu Q, Yao L, Li M, Sun D, Shao Q *et al.*, Ultrasonic pretreated sludge derived stable magnetic active carbon for Cr(VI) removal from wastewater. *ACS Sustain Chem Eng* **6**:7283–7291 (2018). <https://doi.org/10.1021/acssuschemeng.7b04421>.
- Cai W, Wei J, Li Z, Liu Y, Zhou J and Han B, Preparation of amino-functionalized magnetic biochar with excellent adsorption performance for Cr(VI) by a mild one-step hydrothermal method from peanut hull. *Colloids Surf A Physicochem Eng Asp* **563**:102–111 (2019). <https://doi.org/10.1016/j.colsurfa.2018.11.062>.
- Luo C, Tian Z, Yang B, Zhang L and Yan S, Manganese dioxide/iron oxide/acid oxidized multi-walled carbon nanotube magnetic nanocomposite for enhanced hexavalent chromium removal. *Chem Eng J* **234**:256–265 (2013). <https://doi.org/10.1016/j.cej.2013.08.084>.
- Chen T, Xiong Y, Qin Y, Yang H, Zhang P and Ye F, Facile synthesis of low-cost biomass-based γ -Fe₂O₃/C for efficient adsorption and catalytic degradation of methylene blue in aqueous solution. *RSC Adv* **7**:336–343 (2017). <https://doi.org/10.1039/C6RA24900K>.
- Demarchi CA, Michel BS, Nedelko N, Ślawska-Waniewska A, Dłużewski P, Kaleta A *et al.*, Preparation, characterization, and application of magnetic activated carbon from termite feces for the adsorption of Cr(VI) from aqueous solutions. *Powder Technol* **354**:432–441 (2019). <https://doi.org/10.1016/j.powtec.2019.06.020>.
- Silva CC, Melo CA, Soares Junior FH, Moreira AB and Ferreira OP, Effect of the reaction medium on the immobilization of nutrients in hydrochars obtained using sugarcane industry residues. *Bioresour Technol* **237**:213–221 (2017). <https://doi.org/10.1016/j.biortech.2017.04.004>.
- Jia Z, Peng K, Li Y and Zhu R, Preparation and application of novel magnetically separable γ -Fe₂O₃/activated carbon sphere adsorbent. *Mater Sci Eng B* **176**:861–865 (2011). <https://doi.org/10.1016/j.mseb.2011.04.010>.
- Jiang W, Zhang X, Sun Z, Fang Y, Li F, Chen K *et al.*, Preparation and mechanism of magnetic carbonaceous polysaccharide microspheres by low-temperature hydrothermal method. *J Magn Magn Mater* **323**:2741–2747 (2011). <https://doi.org/10.1016/j.jmmm.2011.05.058>.
- Lu AH, Salabas EL and Schüth F, Magnetic nanoparticles: synthesis, protection, functionalization, and application. *Angew Chem* **46**:1222–1244 (2007). <https://doi.org/10.1002/anie.200602866>.
- Zhu X, Liu Y, Qian F, Zhou C, Zhang S and Chen J, Preparation of magnetic porous carbon from waste hydrochar by simultaneous activation and magnetization for tetracycline removal. *Bioresour Technol* **154**:209–214 (2014). <https://doi.org/10.1016/j.biortech.2013.12.019>.
- Zhao N, Wu S, He C, Wang Z, Shi C and Liu E, One-pot synthesis of uniform Fe₃O₄ nanocrystals encapsulated in interconnected carbon nanospheres for superior lithium storage capability. *Carbon* **57**:130–138 (2013). <https://doi.org/10.1016/j.carbon.2013.01.056>.
- Baird RB, Eaton AD and Rice EW, 3500-Cr B. Colorimetric method, in *Standard Methods for the Examination of Water and Wastewater*, ed. by Bridgewater LL. American Public Health Association (APHA), Washington, DC, pp. 3–71 (2017).
- Oliveira I, Blöhsse D and Ramke HG, Hydrothermal carbonization of agricultural residues. *Bioresour Technol* **142**:138–146 (2013). <https://doi.org/10.1016/j.biortech.2013.04.125>.
- Reza MT, Rottler E, Herklotz L and Wirth B, Hydrothermal carbonization (HTC) of wheat straw: influence of feedwater pH prepared by acetic acid and potassium hydroxide. *Bioresour Technol* **182**:336–344 (2015). <https://doi.org/10.1016/j.biortech.2015.02.024>.
- Lu F, Wen L, Li J, Wei J, Xu J and Zhang S, Numerical simulation of iron whisker growth with changing oxygen content in iron oxide using

- phase-field method. *Comput Mater Sci* **125**:263–270 (2016). <https://doi.org/10.1016/j.commatsci.2016.09.003>.
- 30 Sevilla M and Fuertes AB, The production of carbon materials by hydrothermal carbonization of cellulose. *Carbon* **47**:2281–2289 (2009). <https://doi.org/10.1016/j.carbon.2009.04.026>.
 - 31 Liu S, Yao K, Fu LH and Ma MG, Selective synthesis of Fe₃O₄, γ-Fe₂O₃, and α-Fe₂O₃ using cellulose-based composites as precursors. *RSC Adv* **6**:2135–2140 (2016). <https://doi.org/10.1039/C5RA22985E>.
 - 32 de Paula MO, de Tinôco IFF, de Rodrigues CS, da Silva EN and de Souza CF, Potencial da cinza do bagaço da cana-de-açúcar como material de substituição parcial de cimento. *Rev Bras Eng Agrícola e Ambient* **13**:353–357 (2009). <https://doi.org/10.1590/S1415-43662009000300019>.
 - 33 Legodi MA and de Waal D, The preparation of magnetite, goethite, hematite and maghemite of pigment quality from mill scale iron waste. *Dye Pigment* **74**:161–168 (2007). <https://doi.org/10.1016/j.dyepig.2006.01.038>.
 - 34 Salado J, Insausti M, Gil de Muro I, Lezama L and Rojo T, Synthesis and magnetic properties of monodisperse Fe₃O₄ nanoparticles with controlled sizes. *J Non Cryst Solids* **354**:5207–5209 (2008). <https://doi.org/10.1016/j.jnoncrysol.2008.05.063>.
 - 35 Koo KN, Ismail AF, Othman MHD, Bidin N, A Rahman M, Preparation and characterization of superparamagnetic magnetite (Fe₃O₄) nanoparticles: A short review. *Mal J Fund Appl Sci* **15**:1:23–31 (2019). <https://doi.org/10.11113/mjfas.v15n2019.1224>.
 - 36 Zhou X, You S, Wang X, Gan Y, Zhong Y and Ren N, Hydrothermal synthesis of magnetic carbon microspheres for effective adsorption of Cd (II) in water. *J Chem Technol Biotechnol* **89**:1051–1059 (2014). <https://doi.org/10.1002/jctb.4200>.
 - 37 Silverstein RM, Webster FX, Kiemle DJ and Bryce DL, *Spectrometric Identification of Organic Compounds*, 8th edn. John Wiley & Sons, New York, USA, p.464 (2014).
 - 38 Jiang W, Zhang L, Guo X, Yang M, Lu Y, Wang Y et al., Adsorption of cationic dye from water using an iron oxide/activated carbon magnetic composites prepared from sugarcane bagasse by microwave method. *Environ Technol* **42**:337–350 (2019). <https://doi.org/10.1080/09593330.2019.1627425>.
 - 39 Gao Y, Wang X, Wang J, Li X, Cheng J, Yang H et al., Effect of residence time on chemical and structural properties of hydrochar obtained by hydrothermal carbonization of water hyacinth. *Energy* **58**:376–383 (2013). <https://doi.org/10.1016/j.energy.2013.06.023>.
 - 40 Yu G, Sun B, Pei Y, Xie S, Yan S, Qiao M et al., Fe₃O₄@C spheres as an excellent catalyst for Fischer-Tropsch synthesis. *J Am Chem Soc* **132**:935–937 (2010). <https://doi.org/10.1021/ja906370b>.
 - 41 Guo S, Dong X, Wu T, Shi F and Zhu C, Characteristic evolution of hydrochar from hydrothermal carbonization of corn stalk. *J Anal Appl Pyrolysis* **116**:1–9 (2015). <https://doi.org/10.1016/j.jaap.2015.10.015>.
 - 42 Thommes M, Kaneko K, Neimark AV, Olivier JP, Rodriguez-reinoso F, Rouquerol J et al., Physisorption of gases, with special reference to the evaluation of surface area and pore size distribution (IUPAC technical report). *Pure Appl Chem* **87**:1051–1069 (2015). <https://doi.org/10.1515/pac-2014-1117>.
 - 43 Chen B, Yue W, Zhao H, Long F, Cao Y and Pan X, Simultaneous capture of methyl orange and chromium (VI) from complex wastewater using polyethylenimine cation decorated magnetic carbon nanotubes as a recyclable adsorbent. *RSC Adv* **9**:4722–4734 (2019). <https://doi.org/10.1039/C8RA08760A>.
 - 44 Zhou L, Liu Y, Liu S, Yin Y, Zeng G, Tan X et al., Investigation of the adsorption-reduction mechanisms of hexavalent chromium by ramie biochars of different pyrolytic temperatures. *Bioresour Technol* **218**:351–359 (2016). <https://doi.org/10.1016/j.biortech.2016.06.102>.
 - 45 Dobosz B, Krzymiński R, Schroeder G and Kurczewska J, Electron paramagnetic resonance as an effective method for a characterization of functionalized iron oxide. *J Phys Chem Solid* **75**:594–598 (2014). <https://doi.org/10.1016/j.jpcs.2014.01.013>.
 - 46 Griscom DL, Ferromagnetic resonance of precipitated phases in natural glasses. *J Non Cryst Solids* **67**:81–118 (1984). [https://doi.org/10.1016/0022-3093\(84\)90142-X](https://doi.org/10.1016/0022-3093(84)90142-X).
 - 47 Barbata VB, Jardim RF, Kiyohara PK, Effenberger FB and Rossi LM, Magnetic properties of Fe₃O₄ nanoparticles coated with oleic and dodecanoic acids. *J Appl Phys* **107**:073913 (2010). <https://doi.org/10.1063/1.3311611>.
 - 48 Lima E, Brandl AL, Arelaro AD and Goya GF, Spin disorder and magnetic anisotropy in Fe₃O₄ nanoparticles. *J Appl Phys* **99**:083908 (2006). <https://doi.org/10.1063/1.2191471>.
 - 49 Zhang X, Zhang L and Li A, Eucalyptus sawdust derived biochar generated by combining the hydrothermal carbonization and low concentration KOH modification for hexavalent chromium removal. *J Environ Manage* **206**:989–998 (2018). <https://doi.org/10.1016/j.jenvman.2017.11.079>.
 - 50 Ahmed MJK and Ahmaruzzaman M, A facile synthesis of Fe₃O₄-charcoal composite for the sorption of a hazardous dye from aquatic environment. *J Environ Manage* **163**:163–173 (2015). <https://doi.org/10.1016/j.jenvman.2015.08.011>.
 - 51 Qiu B, Gu H, Yan X, Guo J, Wang Y, Sun D et al., Cellulose derived magnetic mesoporous carbon nanocomposites with enhanced hexavalent chromium removal. *J Mater Chem A* **2**:17454–17462 (2014). <https://doi.org/10.1039/C4TA04040F>.
 - 52 Langmuir I, The constitution and fundamental properties of solids and liquids. Part I. Solids. *J Am Chem Soc* **38**:2221–2295 (1916).
 - 53 Fründlich HMF, Über die adsorption in losungen. *Z Phys Chem* **57**:385–471 (1906). <https://doi.org/10.1515/zpch-1907-5723>.
 - 54 Dong X, Ma LQ and Li Y, Characteristics and mechanisms of hexavalent chromium removal by biochar from sugar beet tailing. *J Hazard Mater* **190**:909–915 (2011). <https://doi.org/10.1016/j.jhazmat.2011.04.008>.
 - 55 Kazemi E, Mohammad A, Shabani H and Dadfarnia S, Speciation and determination of chromium ions by dispersive micro solid phase extraction using magnetic graphene oxide followed by flame atomic absorption spectrometry. *Int J Environ Anal Chem* **97**:1080–1093 (2017). <https://doi.org/10.1080/03067319.2017.1381693>.
 - 56 Abilio TE, Soares BC, José JC, Milani PA, Labuto G and Carrilho ENVM, Hexavalent chromium removal from water: adsorption properties of in natura and magnetic nanomodified sugarcane bagasse. *Environ Sci Pollut Res* **28**:24816–24829 (2021). <https://doi.org/10.1007/s11356-020-11726-8>.